

High-resolution energy analysis of field-assisted photoemission: A spectroscopic image of hot-electron transport in semiconductors

J. Peretti, H.-J. Drouhin, and D. Paget

Laboratoire de Physique de la Matière Condensée, Ecole Polytechnique, 91128 Palaiseau, France

(Received 9 March 1992)

Hot-electron transport in indium phosphide is studied by means of energy-resolved field-assisted photoemission of an Ag/InP Schottky diode. The work function of the thin silver top layer is lowered by cesium and oxygen coadsorption. A quasimonoelectronic electron distribution is created close to the bottom of the conduction band in the bulk of the weakly doped p -type InP crystal by near-band-gap light excitation. The energy-distribution curves of the photoemitted electrons are measured for different values of the bias applied to the Ag/InP contact. It is demonstrated that this set of photoemission spectra constitutes a direct measurement of the evolution of the initial distribution during transport in the high electric field of the band-bending region. From this spectroscopic image of the complex multivalley transport, the relevant energy and momentum relaxation processes are clearly identified. Simple models based on the energy balance between the gain in the electric field and the losses by phonon emission account remarkably well for the experimental results. From the comparison between theory and experiment, the characteristic phonon-scattering times are deduced throughout the first conduction band.

I. INTRODUCTION

Field-assisted (FA) photoemission experiments were performed already in the early 1960s to study hot-electron transport in semiconductors.¹ Since the discovery of negative electron affinity (NEA) in 1965,² the lowering of the vacuum level by Cs and O₂ coadsorption has opened a wide field of applications for FA photoemission techniques as probes of high-field hot-electron transport in semiconductors.

FA photoemission of cesiated metal-semiconductor structures was performed by Itoh *et al.* in 1967 on an Al/ p -type-Si Schottky diode.³ These authors measured the dependence of the photoemission quantum yield and of the energy-distribution curves⁴ (EDC's) versus reverse bias applied to the junction under near-band-gap light excitation. More recently, Shariary, Schwank, and Allen have measured the EDC's of electrons emitted into vacuum from a cesiated shallow silicon p - n junction reversely polarized.⁵ Varying the thickness of the n -type layer and the bias applied to the diode, they measured characteristic electron energy losses. They deduced electron escape depths and mean free paths associated with ionization and optical-phonon emission. But, because the measured EDC's were featureless, a complete understanding of the transport properties could not be achieved. In the 1970s, FA photoemission experiments on cesiated Ag/InP Schottky diodes were performed.⁶⁻⁸ On these model FA photocathodes, NEA was achieved at equilibrium (with zero applied bias). With the use of Monte Carlo methods the EDC's of the photoemitted electrons were calculated. From these numerical results, *total* quantum yield measurements were analyzed, and the crucial role played by *intervalley transfer* in high-field transport properties was demonstrated.

When compared to standard current-versus-bias measurements, whose interpretation is intricate because many

different mechanisms are involved and the electron current is related only to the anisotropic part of the electron distribution, the energy-resolved photoemission techniques provide direct information. Nevertheless, because of the lack of energy resolution over a large energy range, previous experiments did not allow making full profit of the FA photoemission capabilities.

Very-high-resolution energy analysis of near-band-gap photoemission from NEA semiconductors has proven to be a valuable tool to investigate band structure and hot-electron transport.^{9,10} This technique, when applied to a FA photoemitter, provides a precise and *direct* spectroscopic image of electron transport under high electric field, inside the semiconductor crystal. First results were briefly presented in Ref. 11. The present paper gives a detailed description of the relevant experimental and theoretical aspects. Our measurements are performed on an Ag/InP Schottky diode. When an increasing reverse bias is applied to the junction, several contributions of significant physical meaning appear in the photoemission spectra. Their behaviors during transport in the high electric field of the band-bending (BB) region evidence different transport regimes: quasiballistic transport in the central (Γ_0) valley of the first conduction band, very efficient intervalley transfer from the central valley to the side valleys, quasistationary transport in the side valleys, and also quasistationary transport in the vicinity of a relative maximum of the second conduction band. This direct image of the evolution of the electron distribution in the crystal allows the description of high-field transport phenomena by simple and physical models in which we analyze the energy balance between the gain in the electric field and the loss by phonon emission. From this analysis, which accounts remarkably well for the experimental results, we deduce estimates of phonon emission times in an energy range which spans the whole energy width of the first conduction band. We also obtain infor-

mation on the semiconductor band structure such as the energy positions of the subsidiary minima L_6 and X_6 of the first conduction band and X_{7c} of the second conduction band, which agree with previous near-band-gap photoemission measurements that we have performed.¹²

II. PRINCIPLES

Cesium and oxygen coadsorption on the clean surface of a semiconductor lowers the vacuum level to about 1 eV above the Fermi level (an energy of the order of the work function of the deposited cesium oxide). For p -type semiconductors with a large band-gap energy, a situation of so-called NEA is created where the vacuum level lies at an energy lower than that of the bottom of the conduction band in the *bulk* solid.² Then, all the electrons promoted from the valence band into the conduction band of the bulk crystal by absorption of near-band-gap light can be emitted into vacuum, resulting in a very high photoemission quantum yield. A typical case is the commercial GaAs photomultiplier tube which is very efficient in the visible and near-infrared region; in this application, highly doped materials, in the 10^{19}-cm^{-3} range, are used in order to avoid energy relaxation in the very thin BB region (about 100 Å wide, i.e., smaller than a typical electron mean free path).¹⁰

The photoelectric response of a NEA photoemitter is only limited, at low energy, by the band-gap energy of the material. When semiconductors with band gaps smaller than about 1 eV are used, a NEA situation can no longer be achieved, resulting in a much lower efficiency at threshold. To overcome this basic limitation, an idea is to use a Schottky diode consisting of a p -type semiconductor of moderate doping level (about 10^{16} cm^{-3}) covered by a thin metal layer.⁶⁻⁸ Such a thin layer is quasitransparent to low-energy electrons and also to infrared and visible light, which allows a reflection-mode operation. By applying a reverse bias to the metal-semiconductor structure (i.e., biasing the metal positively with respect to the semiconductor), the vacuum level is lowered with respect to the energy levels in the *bulk* semiconductor, so that a situation analogous to NEA is created. The low doping level insures good electrical properties. The potentialities of such a device as an infrared detector were demonstrated first on a model system consisting of a p ($\sim 10^{16}\text{ cm}^{-3}$) InP crystal covered by a thin silver layer (of the order of 100 Å). The work function of the silver layer is lowered by Cs and O₂ deposition (the Ag-O-Cs system has some analogies with the standard S-1 photocathode of low work function). More complicated structures have then been used to obtain photoemission at larger wavelength.^{13,14}

Concerning fundamental physics, FA photocathodes are very attractive systems to investigate electron-transport properties. In our experiment, absorption of light of near-band-gap energy creates a very narrow electron energy distribution close to the bottom of the conduction band in the *bulk* semiconductor (because the optical-absorption length is larger than the BB region width). This provides well-defined initial conditions for subsequent transport. These electrons are injected into

the BB region for which the amplitude and width are varied by adjusting the electrical bias applied to the metal-semiconductor junction and accelerated by the electric field towards the surface. There, they gain kinetic energy from the field but at the same time undergo energy relaxation mainly through emission of optical phonons. Finally, they reach the metal-semiconductor interface and cross the metal layer to be emitted into vacuum where their EDC is measured.

The interpretation of the experimental results is supported by the following picture: In a parabolic BB, the energy $\epsilon_c(z)$ of the bottom of the conduction band versus position, referred to the bottom of the conduction band in the bulk, is

$$\epsilon_c(z) = -eV_b(z/w_0)^2, \quad (1)$$

where e is the electron charge, w_0 and eV_b are, respectively, the BB width and amplitude at zero external bias (V_b is taken negative as bands are bent downwards in the space-charge region of a p -type semiconductor); and z is the abscissa measured along the normal to the surface taking the origin at the bulk/BB interface. When a bias V is applied to the Ag/InP Schottky junction, the BB width becomes

$$w = w_0[(V + V_b)/V_b]^{1/2}$$

(V is taken negative for a reverse polarization of the junction). Because an increase of the reverse bias increases the BB width without changing the BB parabolic shape, one can alternately identify the effect of a reverse bias with a displacement of the surface towards the vacuum

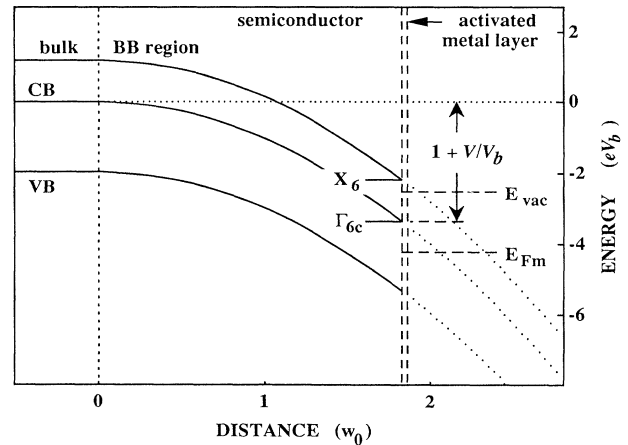


FIG. 1. Band diagram, in real space, of a semiconductor (covered by a thin metal layer) showing the valence-band maximum (VB), the conduction-band minimum (CB), and the X_6 secondary conduction minimum. The band energies are drawn in the BB region (in eV_b units) up to an arbitrary distance from the bulk semiconductor (in w_0 units, where w_0 is the BB width at zero external bias) to illustrate that a change in the bias potential is equivalent to a displacement of the surface. The metal Fermi level and the vacuum level are, respectively, labeled E_{Fm} and E_{vac} . They are pinned to the surface band position. The inset shows the equivalent electrical circuit.

side, the origin being taken inside of the semiconductor, at the bulk/BB interface. This is illustrated in Fig. 1. Therefore, the set of EDC's measured at emission for different values of the bias voltage gives an insight into the evolution of the initial EDC with distance in the BB region.

In the experiment presented here, we have used an InP monocrystal of *p*-doping level $1.2 \times 10^{16} \text{ cm}^{-3}$, oriented along the [100] direction, with a 100-Å-thick Ag top layer activated according to the standard procedure.⁹ For this doping level, the BB region has a width $w_0 = 2900 \text{ Å}$ at zero external bias and we have used biases up to 2.3 V, yielding BB widths up to about 6000 Å. The photocathode is cooled down to 120 K through liquid nitrogen circulation and irradiated by a 1.46-eV-laser-diode light, an energy just exceeding that of the InP band gap $E_G = 1.405 \text{ eV}$ (at 120 K).¹⁵ Therefore, the most energetic electrons are promoted into the conduction band of the *bulk* semiconductor, with a small kinetic energy $\epsilon_{ex} \approx 0.045 \text{ eV}$. But, due to energy relaxation in the bulk semiconductor, the steady-state distribution injected in the BB region is even narrower.

III. EXPERIMENTAL SETUP AND PROCEDURE

The experiments presented here are performed in an ultrahigh-vacuum setup drawn in Fig. 2, composed of three coupled chambers: an introduction lock with a glove box under neutral atmosphere, a preparation chamber where sample heat cleaning, metallization, and surface treatment are carried out, and an energy-analysis

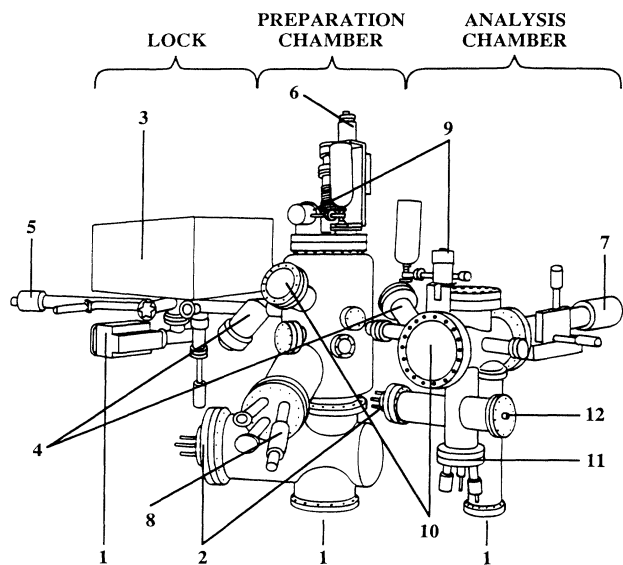


FIG. 2. Experimental setup: 1, ion pumps; 2, titanium sublimator; 3, glove box; 4, isolation valve; 5, sample-transfer system; 6 and 7, z, θ and x, y, z, θ manipulators of the sample holders; 8, Knudsen effusion cell; 9, leak valve for oxygen introduction; 10, window for sample irradiation; 11, electron spectrometer; and 12, Faraday-cup output.

chamber where the EDC's of the photoemitted electrons are recorded at 120 K as a function of the bias voltage applied to the Schottky contact.

A. Sample preparation

It is well known that the quality of NEA photocathodes is crucially dependent on the surface chemistry. Then, the definition of a sample-preparation procedure is of extreme importance but remains largely empirical, the only good final criterion being the photoemissive sensitivity.¹⁶ Concerning FA Schottky photocathodes, the requirements on the surface and interface are even more stringent. Indeed, good electrical properties of the metal-semiconductor contact as well as good photoemissive properties have to be obtained. It is therefore mandatory to start from a clean semiconductor surface and to perform the whole experimental process under very low-pressure conditions.

When working with InP, a difficulty is to obtain an oxygen-free surface because oxygen cannot be thermally desorbed without deeply altering the surface composition. In the procedure we use, the InP crystal is chemically etched in a 0.3% bromine-methanol solution, decanted with isopropanol, and introduced, through a glove box under neutral atmosphere, into the introduction lock. After a short pumping time, the pressure in the lock is lowered down to about 10^{-6} Torr. The sample is then transferred into the preparation chamber where the pressure is routinely kept in the low 10^{-11} -Torr range. This introduction procedure, which takes about half a day, is a way to protect the sample against surface contamination by oxygen.

In this second chamber, the crystal is heat cleaned at 620 K, a temperature which preserves the InP surface stoichiometry. A 100-Å-thick Ag layer is deposited on the clean (100) surface of the InP substrate at a rate of about 1 Å s^{-1} . The low-power ($\approx 50\text{-W}$) Knudsen effusion cell that we have designed operates at this evaporation rate while the pressure remains lower than 2×10^{-10} Torr. Sample contamination during the Schottky-junction elaboration is therefore avoided. The sample temperature during deposition is 300 K. In these conditions, we can assume that the three-dimensional growth of silver on InP has already reached coalescence for a thickness layer of 100 Å.^{17,18} Electrical continuity of the metal layer is achieved anyway (which is already the case with a 50-Å-thick layer⁷), and no significant access resistance is observed as checked by electrical characterization and photoemission measurements. We have shown that such a thin metal layer is quasitransparent to low-energy electrons in the sense that it does not affect the shape of the electron EDC's.¹²

The metal-surface work function is lowered by coadsorption, at room temperature, of cesium (about one monolayer evaporated from a commercial dispenser) and oxygen (introduced into the vacuum chamber through a leak valve). The activation procedure is controlled by optimizing the total photoemission current under He-Ne laser-light excitation at energy 1.96 eV. The typical photoemission quantum yield obtained in these conditions is

of about 0.1% at zero external bias and of about 0.4% when a reverse bias $V = -2.3$ V is applied to the Ag/InP junction. The spectral response of the photocathode (the photoemission quantum yield as a function of the excitation energy) shows that the sample has been activated to "NEA," that is to say, at zero external bias, the vacuum level lies below the bottom of the conduction band in the bulk semiconductor.

The sample is then transferred from the preparation chamber to the analysis chamber where the high-resolution energy analysis of the photoemitted electrons is performed as a function of the bias voltage applied to the Ag/InP Schottky diode. The pressure in the analysis chamber is maintained below 10^{-11} Torr. These ultra-high-vacuum conditions prevent surface contamination and therefore ensure stability of the photocathode for several weeks.

B. Energy analysis

The photoelectrons are energy-selected by a high-performance electron spectrometer developed by Drouhin *et al.* and described in details in Refs. 9 and 19. Here, we briefly give some important characteristics of this analyzer and recall its main performances. The photocathode is facing a 90° cylindrical electrostatic deflector, the rotator, which allows sample illumination normal to the surface. After deflection in the rotator, the electron beam enters a decelerating electron optics which focuses the beam at the entrance of another 90° electrostatic cylindrical deflector where the electrons are energy-selected. The spectrometer operates in the constant-energy mode: The potentials of the spectrometer electrodes remain constant while the cathode potential is scanned (the constant bias of the Ag/InP diode is maintained by applying the scanning potential to the front contact on the silver layer, and a polarization potential between the Ag layer and the back contact of the sample). The sample is located at about 5 mm of the anode hole of 4 mm diameter. Therefore, we have elaborated 8×8 mm² Schottky diodes to avoid disturbing effects of the back contact potential on the EDC of the photoemitted electrons. In proper working conditions, the spectrometer provides a transmission of a few 10^{-3} , constant with electron energy, and a peak output current up to 5 nA, for a 20-meV energy resolution. This resolution is achieved for a selector path energy of 0.5 eV (i.e., the kinetic energy of the electrons in the selector).

C. Absolute energy calibration and BB amplitude determination

The EDC's presented in this paper give a direct spectroscopic image of electron transport in the semiconductor conduction band, through the BB region high electric field. In order to perform a quantitative analysis of the energy-loss mechanisms (phonon-scattering processes) involved during transport, we have to know, with an accuracy better than a typical phonon energy (i.e., ≈ 40 meV),²⁰ for each value of the bias voltage, the following: (i) the kinetic energy of the electrons in the conduction

band of the semiconductor at the interface, i.e., just before emission; and (ii) the *BB amplitude at emission*, which provides the injection energy and also the distance traveled by the electrons from the injection point.

1. Energy calibration

As shown in Fig. 3, when the BB amplitude is small, a peak is observed on the high-energy side of the spectra with a position depending only on the excitation energy (independent of the diode bias voltage). This signal originates from electrons excited in the silver layer. Its high-energy edge corresponds to electrons photoemitted without any energy loss from the Fermi level. Then it provides an absolute reference on the energy scale determining the energy $E_F + h\nu$.

2. BB amplitude determination

As defined in Sec. II, the BB amplitude is $e(V + V_b)$, where eV_b , the BB amplitude at zero bias, is the Ag/InP barrier height reduced by the energy difference between the Fermi level and the top of the valence band in the bulk semiconductor.

(a) *Measurement of the Schottky-barrier height.* We measured the effective Schottky-barrier height ϕ_b using the photoelectric method, the so-called Fowler plot.²¹ This experiment consists of measuring the internal photocurrent I_{ph} which crosses the Schottky junction as a

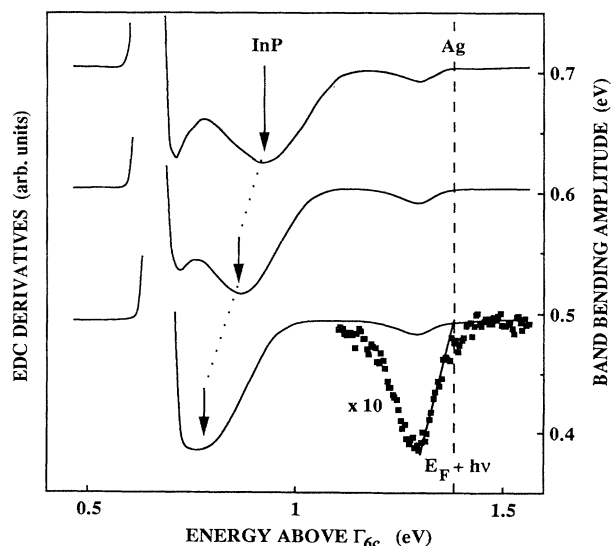


FIG. 3. EDC derivatives recorded at 120 K, with $h\nu = 1.96$ eV excitation energy, for three different values of the bias applied to the Ag/InP junction. The electron energy is referred to Γ_{6c} (the bottom of the conduction band) at the Ag/InP interface. These curves clearly show a bias-dependent feature corresponding to electrons emitted from the InP crystal and a bias-independent photoemission signal originating from the Ag layer. The dotted curve is a ten-time magnification of the Ag-photoemission signal evidencing the sharp high-energy threshold which defines the absolute energy reference $E_F + h\nu$.

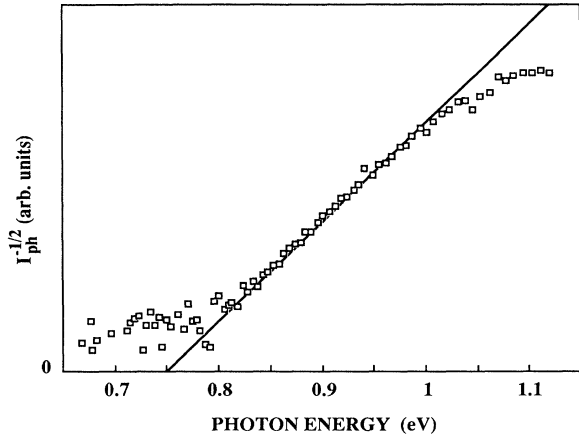


FIG. 4. Fowler plot for Ag/InP Schottky-barrier determination.

function of sub-band-gap light excitation energy. If we call E_G the semiconductor band-gap energy, it can be shown that, for $0 \leq h\nu - e\phi_b \ll E_G - e\phi_b$:

$$I_{\text{ph}}^{1/2} \approx C(h\nu - e\phi_b), \quad (2)$$

where C is a constant.

Equation (2) can be easily derived, assuming conservation of the wave vector parallel to the interface in the internal photoemission process. Practically, this result seems to be very general and the Fowler plot is widely used as a precise technique to determine metal-semiconductor barrier heights.²²

Plotting the square root of the internal photocurrent versus $h\nu$, we indeed observe a linear variation (Fig. 4). The extrapolation of the straight line to $I_{\text{ph}}^{1/2} = 0$ yields $e\phi_B = 0.75$ V. The value of the BB amplitude at equilibrium eV_b is then simply obtained by correcting the measured value of $e\phi_B$ which is underestimated because of the effect of the electron "image potential" (≈ 25 mV) (Ref. 22) and subtracting the energy difference between the Fermi level and the top of the valence band in the bulk of the semiconductor crystal (≈ 55 meV). This yields $eV_b = 0.72$ eV, at 120 K.

(b) *Voltage calibration.* The sample is attached to a tantalum sheet by two metal clamps. The clamps are electrically isolated from the tantalum sheet. They ensure the front electrical contact on the evaporated silver layer while the tantalum sheet ensures the electrical back contact. The Schottky diode is polarized by applying a bias voltage between the clamps and the tantalum sheet. The current-voltage characteristics of the sample, reproduced in Fig. 5, are recorded at 120 K in the dark [curve (a)] and under light excitation [curve (b)]. The shape of these characteristics is not what would be expected from an ideal Schottky photodiode.

In fact, in the experiment reported here, the use of an Ohmic back contact was not easily compatible with our cleaning procedure and experimental configuration. Therefore, the back contact was taken through the simple mechanical contact between the tantalum sheet and the

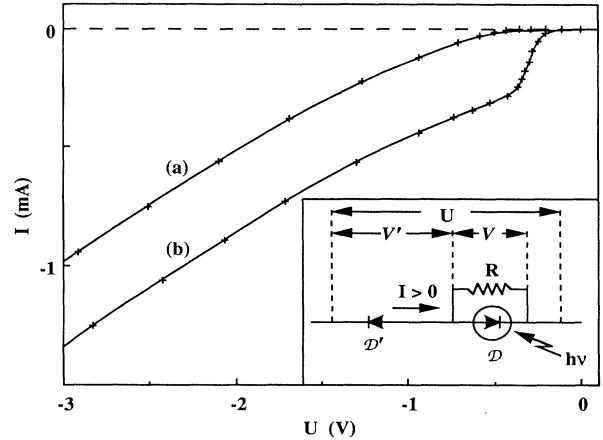


FIG. 5. $I(U)$ curves recorded at 120 K in the dark [curve (a)] and under light excitation at energy 1.46 eV [curve (b)]. The equivalent electrical circuit of the sample is drawn in the inset. The points represented by the symbol + are calculated after the calibration procedure described in detail in Appendix A.

back of the clamped InP substrate of low doping level and was consequently a rectifying contact. In such conditions it is then clear that the bias U applied between the silver layer and the tantalum sheet is not equal to V , the potential actually dropped at the Ag/InP interface.

Our sample is indeed not a pure Schottky photodiode but can be modeled by the equivalent electrical circuit drawn in Fig. 5 (inset). This circuit is composed of a diode \mathcal{D}' (the rectifying back contact), of a photodiode \mathcal{D} (the Ag/InP structure), and of a resistance R parallel to \mathcal{D} . The stray resistance R is probably induced by defects formed at the edge of the sample or at the Ag/InP interface, possibly during the chemical etching and heat cleaning of the InP substrate and/or during the growth of the silver layer and of the cesium oxide. This resistance also introduces into the electrical characteristics of our sample deviations from the characteristics of a simple Schottky photodiode.

When performing a photoemission experiment, \mathcal{D} works as a photodiode. Therefore, important induced photovoltage effects, revealed because of the rectifying back contact, have to be taken into account for proper determination of the voltage actually dropped at the Ag/InP contact.¹¹ Such an effect was also recently considered in photoemission experiments using synchrotron radiation.²³

The large size of the Ag layer required for accurate energy analysis (see Sec. III B) is responsible for a non-negligible additional diode dark current at notable bias, which may significantly affect the electrical characteristics of the sample.

In these conditions, we performed a careful analysis of the current-voltage characteristics of our modeled structure, in the dark and under illumination. The current-voltage characteristics of the equivalent circuit calculated after this analysis are plotted in Fig. 5 (symbol +). They closely fit the experimental results. This voltage-calibration treatment, detailed in Appendix A, allows the

determination of the true electrical bias V applied to the Ag/InP diode with an accuracy better than the energy resolution. From now on, all the values of the bias V [i.e., of the BB amplitude $e(V + V_b)$] are obtained using this procedure.

IV. EXPERIMENTAL RESULTS

EDC's of FA photoemission are shown in Fig. 6. Electron energy is referred to the bottom of the conduction band at the Ag/InP interface, labeled Γ_{6c} . Along the ordinate axis, the curves are shifted by $e(V + V_b)$. At low BB amplitude, the small photoemission signal essentially originates from the Ag layer and was used for energy calibration. Applying a sizeable reverse bias allows electron emission from the semiconductor, which strongly improves the photoemission quantum yield (up to 0.4% at the highest reverse bias, i.e., the largest BB amplitude, that we consider in Fig. 6). A further increase of the re-

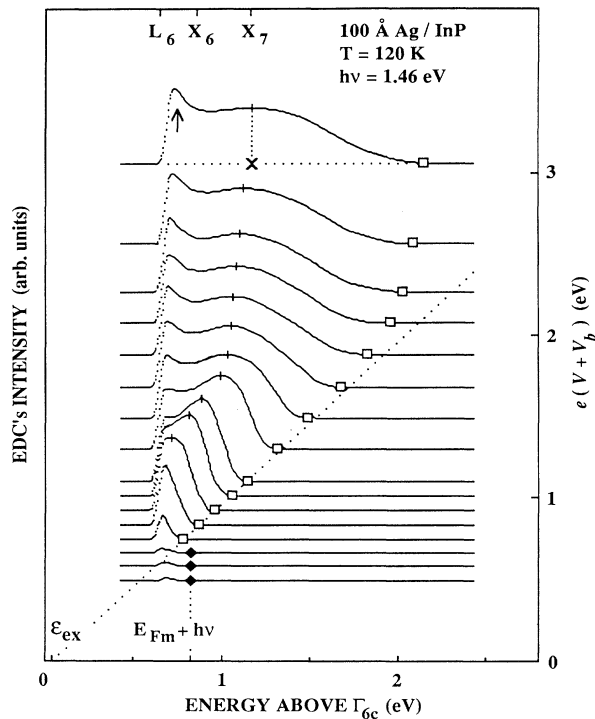


FIG. 6. EDC's at different bias potentials. The electron energy is referred to Γ_{6c} (the bottom of the CB) at the Ag/InP interface. The positions of the relevant conduction-band minima at the interface are indicated on the upper horizontal axis. The curves are normalized so that their area is proportional to the total emitted current. On the vertical scale (right), they are shifted by the BB amplitude, $e(V + V_b)$. The symbols \square and \times refer, respectively, to the EDC's high-energy edge and to the main-peak maximum (indicated by a vertical bar). The low-energy contribution (\uparrow), due to electrons partially relaxed near the Ag/InP interface, is not considered in the discussion. The equation of the dotted straight line is $\epsilon = \epsilon_{ex} + e(V + V_b)$. The high-energy edges of the three lowest EDC's (\blacklozenge) correspond to electrons excited from the Ag Fermi level.

verse bias produces spectacular modifications of the electron energy distribution. On these EDC's or on their derivatives (Figs. 7–9) we distinguish several particular features, as follows, which have a physical meaning with respect to transport properties of InP.

(i) *The high-energy edge of the spectra* (symbol \square in Fig. 6). For low values of the BB amplitude, this threshold, plotted versus $e(V + V_b)$, is located on a straight line of slope 1. When $e(V + V_b)$ exceeds 1.70 eV, its position tends to saturate at an energy of about 2.15 eV.

(ii) *The maximum of the main photoemission peak* (symbol \times in Fig. 6). It corresponds to electrons initially thermalized at the bottom of the conduction band, in the bulk semiconductor, and subsequently heated in the BB region electric field during transport towards the surface. The energy position of this peak varies linearly versus $e(V + V_b)$ with a slope almost equal to unity when $e(V + V_b)$ varies from 0.92 up to 1.22 eV. Below $e(V + V_b) = 0.92$ eV, this peak cannot be observed as it should lie under the vacuum level. When $e(V + V_b) > 1.22$ eV, the main peak becomes broader and its energy position still varies linearly, but with a slope as small as 0.1.

(iii) *The structures observed in the derivatives of the EDC's* (marked by arrows in Figs. 7–9). They only appear for notable values of the bias voltage, and their posi-

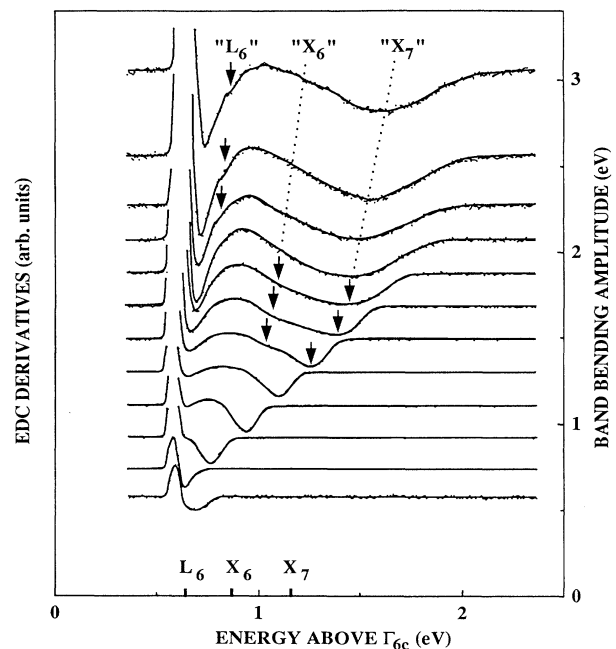


FIG. 7. Derivatives of some EDC's recorded under bias conditions such that extra structures are revealed. These structures correspond to electrons emitted from side valleys. The electron energy is referred to Γ_{6c} (the bottom of the CB) at the Ag/InP interface. The positions of the relevant conduction-band minima at the interface are indicated on the horizontal axis. On the vertical scale (right), they are shifted by the BB amplitude, $e(V + V_b)$. The appearance of features, indicated by arrows, evidences electron transport in the side valleys.

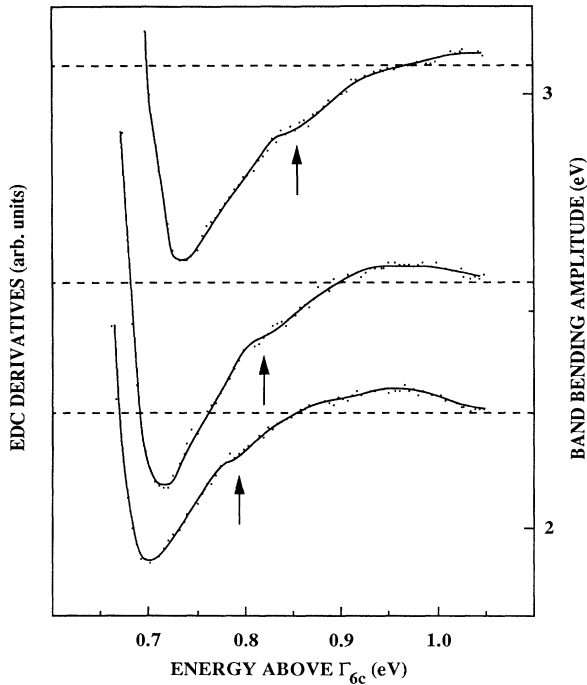


FIG. 8. Enlargement of EDC's derivatives recorded at high-reverse voltages. They show a weak but reproducible bias-dependent shoulder corresponding to electrons photoemitted from the L_6 conduction side valleys. The position of the high-energy edge of this structure is plotted in the structure diagram of Fig. 10 (symbol \circ).

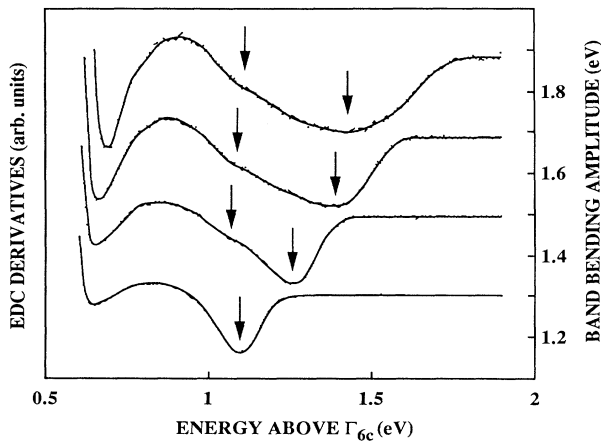


FIG. 9. Enlargement of EDC's derivatives recorded at notable reverse voltages. They show the splitting in two contributions, marked by arrows, of the bias-dependent peak. The contribution at lower energy is attributed to electrons transferred into the X_6 conduction side valleys; the characteristic point of this feature which is used for analysis is the maximum of the corresponding EDC peak (i.e., the relevant zero of the derivative); the position of this point is plotted vs BB amplitude in the FA structure diagram (Fig. 10, symbol \times). The contribution at higher energy corresponds to electrons which first still undergo ballistic transport and then are transferred into the X_{7c} side valleys of the second conduction band. The position of this peak in the derivative is plotted in Fig. 10 (symbol \bullet).

tions vary linearly versus the BB amplitude with a slope of the order of 0.1.

Remark that, at the low-energy cutoff, which corresponds to the vacuum level, an intense peak (marked by an arrow in Fig. 6) appears for $e(V + V_b) \approx 1$ eV and, for higher values, is almost independent of bias. This part of the EDC's is the high-energy tail of the distribution of electrons partially relaxed in the BB region (for instance, those reflected at the surface or at the interface) and which accumulate at the bottom of the conduction band near the Ag/InP interface. No information on transport properties of InP can be directly deduced from this part of the photoemission signal. Therefore, we shall not consider this contribution in the following analysis.

V. ANALYSIS

In order to interpret the experimental data, we draw the FA-photoemission structure diagram in Fig. 10, i.e., we plot the energy location of characteristic points of the features appearing in the spectra or in their derivatives as a function of the BB amplitude. This diagram is analogous to the usual photoemission structure diagram,^{9,12,24,25} the photon energy being replaced here by the BB amplitude. In the following, we consider that electrons only lose energy by phonon emission which is by far, in our experimental conditions (low temperature, low doping level, low carrier density, and low kinetic energy), the dominant scattering mechanism.^{9,16}

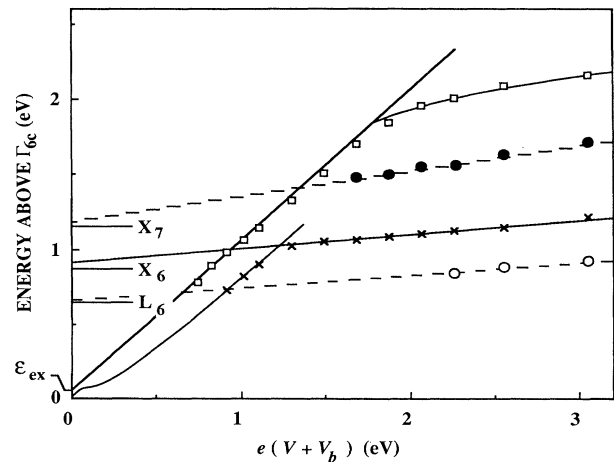


FIG. 10. Field-assisted structure diagram, i.e., plot of the energy position of particular points of the EDC's (or of their derivatives) vs $e(V + V_b)$. The symbols \square and \times represent, respectively, the EDC's high-energy end and the main-peak maximum. The solid lines are the fits discussed in the text. The symbols \circ and \bullet correspond to features only observed on the EDC's derivatives and, respectively, attributed to the L_6 and X_7 valleys; the dotted lines show that the model given for the transport in the X_6 valleys also accounts for the contributions of the other subsidiary minima.

**A. The high-energy edge of the EDC's:
Transport close to a conduction-band maximum**

At the interface, the kinetic energy of the electrons which do not undergo any energy loss during transport from excitation to emission is given by $\varepsilon = \varepsilon_{\text{ex}} + e(V + V_b)$. As mentioned in Sec. IV, paragraph (i), we observe ballistic electrons up to $e(V + V_b) = 1.70$ eV (Fig. 10, symbol \square). Beyond that point, the most energetic electrons that can be observed gain less energy than the increase of the BB amplitude and their energy tends to saturate.

We simply interpret this behavior in the following manner. The electron energy gain is maximum in the direction parallel to the electric field, i.e., in the [100] direction normal to the surface. In this direction, the electrons should attain a band maximum where their group velocity becomes zero. Near this point, the energy losses (by phonon emission) per unit length become so important that the electrons cannot actually reach this maximum. In a one-dimensional model, assuming that electrons have a steady-state energy at each point of the BB region, we can write the energy balance

$$d\varepsilon/dt = (-e)v_G E(z) - \hbar\omega/\tau = 0, \quad (3)$$

where v_G is the electron group velocity, $\hbar\omega$ the typical energy loss in the collision time τ , and $E(z)$ the modulus of the electric field \mathbf{E} at the distance z from the injection point. In a parabolic approximation of the band dispersion near a band maximum at energy ε_0 (wave vector k_0) and along the direction normal to the surface, the kinetic energy can then be written as a function of the wave vector k :

$$\varepsilon(k) = \varepsilon_0 - \hbar^2(k_0 - k)^2/2m^* \quad (4)$$

m^* is the effective-mass component normal to the surface in the vicinity of the band maximum. As τ generally varies slowly with ε , we neglect its variation in the relevant energy range. Then, combining Eqs. (3) and (4), we get at emission ($z = w$):

$$\varepsilon = \varepsilon_0 - (m^*/2)[\hbar\omega/(-e)E(w_0)\tau]^2[V_b/(V + V_b)]. \quad (5)$$

According to this model, the plot of the experimental values of $\varepsilon e(V + V_b)$ as a function of $e(V + V_b)$ should be a straight line. As shown in Fig. 11, from $e(V + V_b) = 2$ eV to $e(V + V_b) = 3$ eV, we indeed observe a linear variation of slope $\varepsilon_0 = 2.56$ eV. This energy corresponds, in fact, to an extremum of the *second* conduction band in the [100] direction, located at about 2.60 eV above the minimum of the conduction band, as given by a band-structure calculation in a pseudopotential model,²⁶ while the maximum of the *first* conduction band lies 0.50 eV lower, at 2.10 eV. Evidence that electrons are transferred into the second conduction band is supported by the observation of a high-energy feature in the EDC's derivatives, which we identify with electrons emitted from the *second* conduction-band minimum X_7 (Figs. 7 and 9). Moreover, before the saturation regime, one can observe (Fig. 12), on the variation of the high-energy threshold of the spectra, a small energy loss (≈ 40 meV)

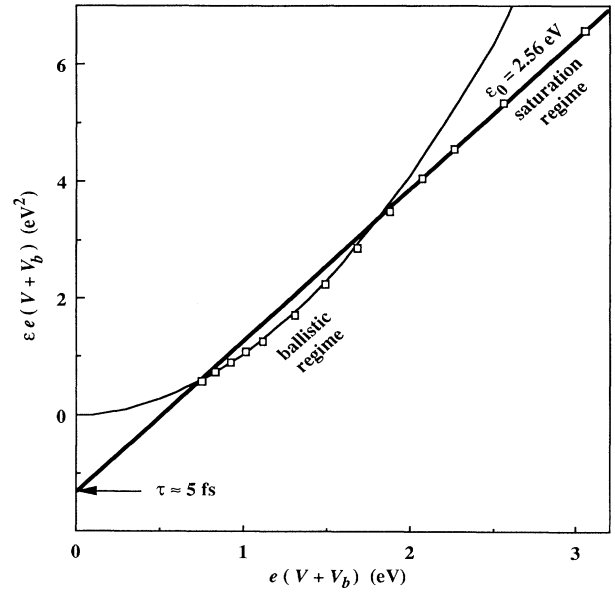


FIG. 11. Plot of the product $\varepsilon e(V + V_b)$, where ε is the energy position of the EDC's high-energy threshold, vs $e(V + V_b)$. This evidences the linear saturation regime which occurs close to a relative maximum of the conduction band as predicted by Eq. (5). The parabola corresponds to ballistic electrons.

occurring at $\varepsilon \approx e(V + V_b) \approx 1.3$ eV, an energy about 100 meV higher than the minimum X_7 of the *second* conduction band in the [100] direction (see Sec. VC of the present paper and Ref. 12). This energy loss can therefore be interpreted as phonon emission related to the transfer from the first to the second conduction band.

Finally, from the extrapolation of the straight line giving $\varepsilon e(V + V_b)$ versus $e(V + V_b)$ to $e(V + V_b) = 0$, we obtain

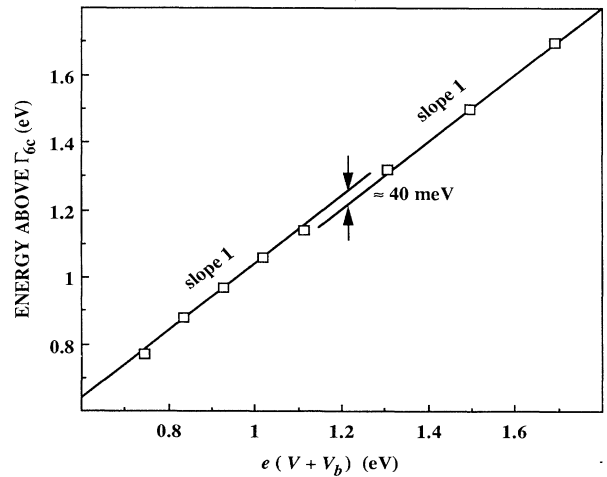


FIG. 12. Plot of the energy position of the EDC's high-energy end vs $e(V + V_b)$ in the range where ballistic transport is observed. The 40-meV energy loss occurring at about 1.2 eV indicates phonon emission associated with intervalley transfer.

$$(m^*/2)[\hbar\omega/(-e)E(w_0)\tau]^2eV_b=1.4\text{ eV}^2.$$

From this value, taking $\hbar\omega=40\text{ meV}$, a typical phonon energy,²⁰ and $m^*=0.2m_0$ (Ref. 26) (m_0 is the free-electron mass), we deduce $\tau\approx 5\text{ fs}$. It is not surprising that we do not observe ballistic electrons with such a short phonon emission time. Indeed, as we will see in Sec. VB, in the region of the Brillouin zone where a ballistic-transport regime is observed, the collision time is about ten times larger than τ . The variation of ε versus $e(V+V_b)$ given by Eq. (5) is plotted in Fig. 10 using the values of ε_0 and τ that we have obtained.

B. The maximum of the main peak at low bias: Quasiballistic transport in the Γ valley

Quasimonoenergetic electrons are injected, at the bulk/BB interface, in the BB region, and accelerated in the electric field. At the same time, they suffer energy losses mainly by emission of polar optical phonons of energy $\hbar\omega_{\text{op}}$ (in weakly doped III-V semiconductor compounds, polar optical scattering is the most efficient collision process at low kinetic energy in the central Γ valley of the conduction band). In a simple parabolic band model, the corresponding collision time τ_{op} varies with ε (for $\varepsilon\geq\hbar\omega_{\text{op}}$) according to²⁷

$$1/\tau_{\text{op}}=(1/\tau_0^*)(\hbar\omega_{\text{op}}/\varepsilon)^{1/2}\sinh^{-1}[(\varepsilon/\hbar\omega_{\text{op}})-1]^{1/2}, \quad (6)$$

where τ_0^* is a characteristic time constant.

It is shown in Appendix B that this formula can be generalized to a more realistic (nonparabolic) conduction-band structure described in the framework of the $\mathbf{k}\cdot\mathbf{p}$ Kane perturbation model²⁸ in the form

$$1/\tau_{\text{op}}=(1/\tau_0^*)(\mathcal{P}/\hbar v_G)\{\sinh^{-1}[(\hbar v_G k/2\hbar\omega_{\text{op}})-1]^{1/2}-2c_6^2(1-c_6^2/2)\times(1-2\hbar\omega_{\text{op}}/\hbar v_G k)^{1/2}\}, \quad (7)$$

where τ_0^* is a characteristic time constant and v_G the electron group velocity. The quantity \mathcal{P} is a real momentum matrix element between valence and conduction states and c_6 a coefficient describing the hybridization of the conduction band in the Kane model.²⁸

For a qualitative insight, the important point is that as soon as the electron kinetic energy is somewhat larger than $\hbar\omega_{\text{op}}$, the efficiency of this relaxation process is nearly constant versus energy. We can then deduce that the electron kinetic energy remains small as long as the energy gain from the electric field in the electron mean free path λ remains smaller than the characteristic energy loss, i.e., $eE\lambda<\hbar\omega_{\text{op}}$. Beyond that point, the transport becomes quasiballistic. Experimentally, we observe a ballistic transport mode for

$$0.92\text{ eV}\leq e(V+V_b)\leq 1.22\text{ eV},$$

where the energy position of the peak, plotted versus $e(V+V_b)$, follows a line of slope almost 1 (Fig. 10). Extrapolating this line to zero kinetic energy shows that quasiballistic transport should start approximately from

$$e(V+V_b)=e(V+V_b)_0=0.15\text{ eV}.$$

This yields $\lambda\approx 200\text{ \AA}$, a value which corresponds to a collision time of the order of 50 fs for an electron of energy somewhat larger than $\hbar\omega_{\text{op}}$.

Now, we remark that, in the quasiballistic regime, the electron kinetic energy increases linearly with the BB amplitude with a slope 0.94. This indicates that these electrons lose 6% of the energy they gain in the field. Therefore, the ‘‘mean electron’’ gains $\frac{100}{6}\hbar\omega_{\text{op}}$ before emitting a phonon. One can then consider that the time necessary for an electron to gain this energy is a good estimate of the polar-optical-phonon emission time. In order to calculate this time, we start from the one-dimensional transport equation

$$d\varepsilon/dt=(1/\hbar)(d\varepsilon/dk)(-e)E. \quad (8)$$

From our assumption, in the energy range where the quasiballistic regime is observed, the kinetic energy before emission of a phonon is given by

$$\varepsilon=e(V+V_b)-e(V+V_b)_0. \quad (9)$$

In a parabolic description of the conduction band of effective mass m_6 , Eqs. (8) and (9) give

$$dt=w_0(m_6/2eV_b)^{1/2}[1/4u(u+1)]^{1/2}du, \quad (10)$$

where u is a reduced variable defined as $u=\varepsilon/e(V+V_b)_0$. The summation over u yields

$$\tau_{\text{op}}=w_0\left[\frac{m_6}{2eV_b}\right]^{1/2}[\ln(\sqrt{u}+\sqrt{u+1})]_{u_1}^{u_2}, \quad (11)$$

where the values of ε corresponding to the boundaries of integration u_1 and u_2 , respectively,

$$\varepsilon_1=1.02\text{ eV}+\hbar\omega_{\text{op}}-100\hbar\omega_{\text{op}}/6$$

and $\varepsilon_2=1.02\text{ eV}+\hbar\omega_{\text{op}}$, are chosen in the energy range where quasiballistic transport is actually observed. We find $\tau_{\text{op}}\approx 70\text{ fs}$.

In order to obtain a more realistic description of the quasiballistic transport throughout the whole BB region in the central Γ valley, we have performed a numerical resolution of the differential transport equation:

$$d\varepsilon/dt=ev_G E(z)-\hbar\omega_{\text{op}}/\tau_{\text{op}}. \quad (12)$$

In this calculation, we assume a one-dimensional transport regime along the direction of the electric field. This assumption is justified because polar-optical-phonon emission favors forward scattering: The probability of an electron being scattered by a polar optical phonon is proportional to $1/q^2$ (where q is the modulus of the phonon wave vector),²⁷ i.e., the smaller q is, the more probable the collision process. We use a nonparabolic description of the conduction band, deduced in the framework of the Kane band model (see Appendix B and Refs. 12 and 29), and Eq. (7) for the expression of τ_{op} . We obtain the variation of ε versus $e(V+V_b)$, which is plotted in Fig. 10. The characteristic time constant τ_0^* is the only adjustable parameter of the model. The agreement with the experimental data is very good for $\tau_0^*=120\text{ fs}$.

$\tau_{\Gamma-X}$ of the order of 20 fs for an electron of saturated group velocity (i.e., in a domain of the Brillouin zone where the conduction-band dispersion is almost linear: $v_G \approx \mathcal{P}/\hbar \approx 10^6$ m s⁻¹ in InP). The fact that this collision time is about three times shorter than τ_{op} explains the high efficiency of the Γ - X transfer process that we observe (see Fig. 13 for comparison).

From our determination of intervalley scattering times $\tau_{\Gamma-X}$, which is consistent with the one measured very recently in GaAs,³⁰ and τ_{iv} , we estimate the intervalley coupling constants $D_{\Gamma X}$ and D_{XX} (Ref. 27) of the order of 1×10^9 eV cm⁻¹, while the values of these quantities reported in the literature are controversial as they range over more than one order of magnitude, typically from 1×10^8 up to 2×10^9 eV cm⁻¹.^{16,31}

In the present FA experiment, the identification of the Γ_6 - X_6 transfer is supported by the observation of features in the EDC's derivatives (Fig. 7) that we identify with electrons emitted from the L_6 and X_{7c} side valleys. The structures corresponding to the L_6 valleys are small but reproducible; they are evidenced in Fig. 8. The structures corresponding to the X_{7c} valleys are observed in Fig. 9 where the peak of transferred electrons is clearly split. As shown in Fig. 10, the variation of the position of these structures as a function of the BB amplitude is in both cases a straight line. Then, the above analysis can also be applied to the L_6 and X_{7c} side valleys. Extrapolating the lines to zero BB amplitude, their respective energy positions are found equal to 0.64 and 1.15 eV in very good agreement with the values of Ref. 12. Of course, as the slopes of the lines are also of the order of 0.1, the intervalley-scattering times that can be deduced from the model are of the same order of magnitude as those calculated for the X_6 side valleys.

VI. CONCLUSION

Field-assisted photoemission is a very attractive technique to investigate hot-electron transport in semiconductors. Its decisive advantage is to provide a direct picture of the electron energy distribution during the motion. Because particular points of the EDC, which have a well-defined physical meaning, can be followed as a function of the electrical bias, a precise quantitative interpretation is possible even using very tractable theoretical tools. Such a situation is in fact much simpler than in usual current-versus-voltage measurements which give a direct access only to the drift velocity, i.e., to the anisotropic part of the EDC; in particular, if multivalley transport is considered, the drift velocity can be very small although the kinetic energy can be important. So in the case of the Ag/InP model system, we are able to disentangle the contributions of the different energy relaxation mechanisms and to estimate relevant relaxation times in a wide energy range; our results clearly evidence the multivalley transport process, which involves the central and side minima of the first conduction band, and also at high bias the second conduction band. Intervalley scattering plays consequently a crucial role and determines important photoemission properties. Moreover, similarly to "standard" NEA photoemission, field-assisted photo-

emission provides a spectroscopic determination of the locations of the different conduction-band minima. This approach would be of particular interest for small band-gap semiconductors which cannot be activated to NEA. Finally, the present work develops an original technique which could also find valuable applications in the study of heterostructures, quantum wells, or superlattices.

ACKNOWLEDGMENTS

We express our deep gratitude to G. Lampel for his continuing interest and significant contribution to the progress of this work. We thank C. Hermann, G. Lampel, and Y. Lassailly for a critical reading of the manuscript. We are grateful to C. Piaget for very valuable discussions during the genesis of the experiment. We thank A.-M. Huber and M. Razeghi for helpful information concerning sample preparation. We are indebted to C. Bréant and C. Salomon for useful advice concerning the optical setup. This work was performed under contract D.R.E.T. No. 87-224. Laboratoire de Physique de la Matière Condensée is "Unité de Recherche 1254 Associée au Centre National de la Recherche Scientifique, France."

APPENDIX A: VOLTAGE CALIBRATION

The current (I)-voltage (U) characteristics of our sample, plotted in Fig. 5, have been recorded at 120 K: curve (a) in the dark, curve (b) under about 3-mW laser-diode excitation at 850 nm. As explained in Sec. III C 2 (b) of the main text, these curves have not the typical shape of Schottky-diode characteristics because the sample is in fact equivalent to the electrical circuit drawn in Fig. 5 (inset). The back electrical contact is rectifying and has to be regarded as a Schottky diode \mathcal{D}' . Defects are responsible for a parasitic resistance (R) parallel to the Ag/InP Schottky photodiode \mathcal{D} .

It is then clear that the current which flows through the circuit defines independently the voltage drops at \mathcal{D} (and R) and at \mathcal{D}' . Therefore, the bias U that we apply to the whole circuit, between the Ag layer and the back contact, is not only dropped at the Ag/InP junction. Note also that, when we perform FA photoemission, the sample is illuminated through the Ag layer. The light absorbed inside the semiconductor close to the Ag/InP interface (the typical absorption length is of the order of a few μ m) induces an internal photocurrent I_{ph} through the junction. In these conditions, when the bias U is such that the total current I which crosses the whole structure tends to zero, the bias of the Ag/InP junction is positive and tends to a direct *effective open-circuit voltage* V_{oc}^* which accounts for the diode characteristics with a current flowing through the load resistance R . The BB amplitude near the Ag/InP interface is then of course reduced by eV_{oc}^* . This photovoltage effect, revealed because of the rectifying back contact, is very important in our experimental conditions (several hundreds of mV).

In the following, we will show that the analysis of the experimental $I(U)$ curves leads to a rather good graphical estimate of the relevant parameters of the equivalent

circuit. In Fig. 14 we indicate the particular points or "regions" in the $I(U)$ curves that we have specifically chosen to perform this analysis. Then, successive numerical treatments of the experimental data, based on the calculation presented below, allow deduction of corrective terms, some depending on the dark current of \mathcal{D} , others depending on the internal photocurrent. Iterations of the whole procedure, taking into account the corrections, quickly converge and improve the estimate of the parameter values. Finally, the numerical resolution of the basic current-voltage equations of the modeled system are performed by calculating, for a given value of the bias V applied to the Ag/InP junction, the value of the bias U applied between the front and the back contacts. This yields the dependence of U versus V from which we obtain the variation of the BB amplitude versus U .

\mathcal{D} and \mathcal{D}' are nonperfect diodes. Their respective ideality factors (saturation currents) are called n (I_0) and n' (I'_0). When \mathcal{D} is reversely polarized, the $I(U)$ curves exhibit a bias-dependent dark current I_d which soon becomes important (because of the large size of the Ag/InP junction) when U increases. If we call V and V' the voltage drops, respectively, at \mathcal{D} (and R) and at \mathcal{D}' , the current-voltage equations are

$$I = I_0[\exp(eV/nkT) - 1] + I_{ph} + I_d + V/R, \quad (\text{A1})$$

$$I = -I'_0[\exp(eV'/n'kT) - 1], \quad (\text{A2})$$

$$U = V - V'. \quad (\text{A3})$$

As will be checked later, I_0 and I'_0 are several orders of magnitude smaller than the value of I at the specific points of the characteristics used to perform this analysis. Therefore, in the following, we will neglect them with respect to I .

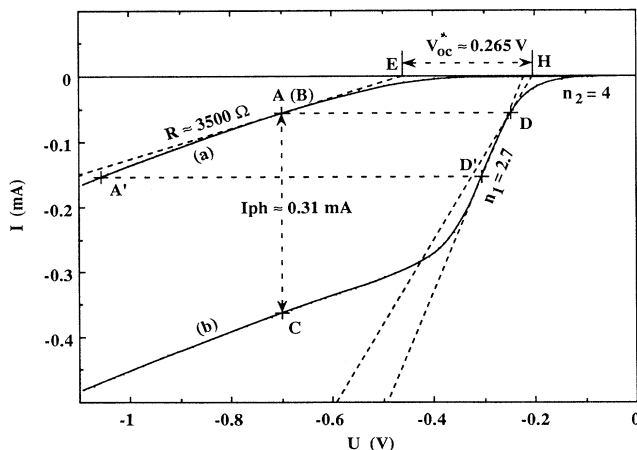


FIG. 14. Experimental $I(U)$ characteristics of the sample recorded *in situ*, curve (a) in the dark and curve (b) under illumination. The principle of the graphic estimate of the parameters of the electrical circuit equivalent to the sample is illustrated. The particular points considered in Appendix A are indicated.

Note that, combining Eqs. (A2) and (A3), we obtain

$$V = U + (n'kT/e)\ln(1 - I/I'_0). \quad (\text{A4})$$

Then, in order to carry out the voltage calibration, one has only to determine n' and I'_0 . Nevertheless, we have to verify the consistency of our calibration procedure by fitting the experimental $I(U)$ curves over the whole voltage range, and this requires the determination of all the parameters of the equivalent circuit.

1. Estimation of n'

Let us first consider the $I(U)$ curve recorded *under illumination* [curve (b) in Fig. 14]. As already mentioned, as long as the current flowing through the device is a small fraction of I_{ph} (typically $I \leq 50 \mu\text{A}$ in the present experiment), V is not very different from V_{oc}^* , and, consequently, from Eq. (A3), we have $V' \approx V_{oc}^* - U$. Therefore, according to Eq. (A2), the variation of $-I$, recorded under light excitation, versus $-U$ in the "small current" range, is essentially the corresponding part of the \mathcal{D}' current-voltage characteristics shifted along the voltage axis by V_{oc}^* . This leads to

$$\ln(-I) \approx \ln(I'_0) - eU/n'kT + eV_{oc}^*/n'kT. \quad (\text{A5})$$

The plot of $\ln(-I)$ versus U , drawn in Fig. 15, is indeed a straight line. From its slope we deduce the value $n' \approx 4$. From its extrapolation to $U=0$, the value of I'_0 can be deduced if V_{oc}^* is known. In Sec. 5 of the present appendix, we will show that V_{oc}^* can be graphically estimated with a good precision as equal to 0.265 V, which yields $I'_0 \approx 1.8 \times 10^{-7}$ mA. For that purpose we will first estimate R , I_{ph} , and n .

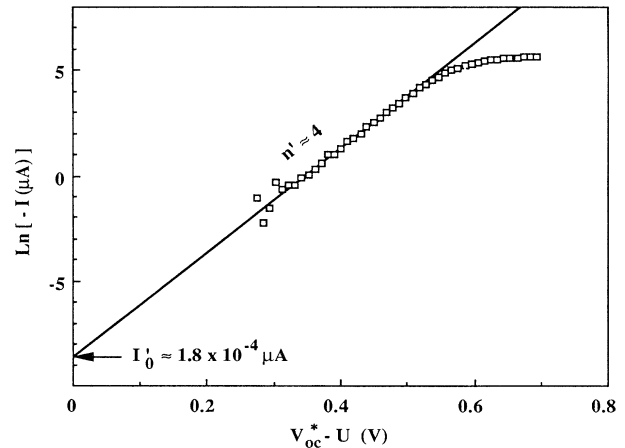


FIG. 15. Plot of the variation of $\ln(-I)$ vs $V_{oc}^* - U$ from the experimental $I(U)$ characteristics of the sample recorded under illumination. As predicted by Eq. (A5), in the low- U range, this curve is a straight line of slope $e/n'kT$ which gives $n' = 4$. The value of V_{oc}^* , used to deduce I'_0 from the extrapolation of the line to $V_{oc}^* - U = 0$, is graphically determined as discussed in Sec. 5 of Appendix A.

2. Estimation of R

Let us consider now the $I(U)$ curve recorded *in the dark* ($I_{\text{ph}}=0$, $V_{\text{oc}}^*=0$). When $U \leq 0$, $V \leq 0$, and I is dominated by the current across R (at least in the region where I is much larger than I_0 and I_d). Then, the slope $Y=(dI/dU)$ of the $I(U)$ curve must strongly depend on R . We note $\alpha=(dI_d/dU)$, and differentiate equations (A1), (A2), and (A3) with respect to U :

$$Y = \{ (e/nkT)[I + I_0 - I_d - V/R] + \alpha + 1/R \} (dV/dU), \quad (\text{A6})$$

$$Y = [e(I - I'_0)/n'kT](dV'/dU), \quad (\text{A7})$$

$$1 = (dV/dU) - (dV'/dU). \quad (\text{A8})$$

When I is much larger than I_0 ,

$$e(I + I_0 - I_d - V/R)/nkT$$

is much smaller than eI_0/nkT and therefore can be neglected. We also neglect I'_0 with respect to I . Then, combining Eqs. (A6), (A7), and (A8), we get

$$R = R'[1 + \alpha/(1/R' - \alpha)], \quad (\text{A9})$$

where $R' = (1/Y + n'kT/eI)$.

In the low-voltage range (typically $-1 \leq U \leq 0$ V), the value of V is low enough that I_d and α are much smaller than, respectively, I and $Y (\approx 1/R')$. Then, in this range we have

$$1 + \alpha/(1/R' - \alpha) \approx 1. \quad (\text{A10})$$

In order to estimate the value of R from Eqs. (A9) and (A10), we choose, on the $I(U)$ curve recorded *in the dark*, a particular point A of coordinates ($U_A = -0.7$ V, $I_A = -0.056$ mA) and measure the slope $Y_A \approx 0.24 \times 10^{-3} \Omega^{-1}$ (Fig. 14). Then we deduce $R \approx 3450 \Omega$.

This determination of R can be pinpointed precisely if the variation of I_d versus V (and therefore α) is known. As n' has been measured, this will be possible provided I'_0 is determined. Indeed, using Eq. (A2), for each value of I we can obtain, from the value of V' and, therefore, from Eq. (A3), the corresponding value of V . Then, using Eq. (A1) and the above value of R , we deduce from the $I(U)$ curve recorded *in the dark* the variation of I_d versus V . Consequently, after determining I'_0 from the procedure described in the next Secs. 3–6 of this appendix, we return to the determination of R at a point A' located at larger bias on the $I(U)$ curve recorded in the dark (for instance, the point of coordinates $U_{A'} = -1.06$ V and $I_{A'} = -0.156$ mA, as drawn in Fig. 14). We measure $Y_{A'}$ and $\alpha_{A'}$ ($Y_{A'} \approx 0.31 \times 10^{-3} \Omega^{-1}$ and $\alpha_{A'} \approx 0.05 \times 10^{-3} \Omega^{-1}$) and we calculate a corrected value of R . Finally, we adjust the R value until its determination at points A and A' coincide. So we obtain $R \approx 3500 \Omega$ and verify that this estimation remains correct at any point of the characteristics.

3. Estimation of I_{ph}

We will now show how to measure I_{ph} that we first consider as a constant in the low-voltage range, $-1 \leq U \leq 0$ V. At point A , I_d takes the value I_{dA} and the biases applied to \mathcal{D} (as well as to R) and to \mathcal{D}' are, respectively, V_A and V'_A :

$$V_A = R(I_A - I_{dA}), \quad (\text{A11})$$

$$V'_A = R(I_A - I_{dA}) - U_A. \quad (\text{A12})$$

We now consider the point C , of the characteristics recorded *under illumination*, of coordinates (U_C, I_C) chosen so that $U_C = U_A$ (see Fig. 14). At this point I_d (I_{ph}) takes the value I_{dC} ($I_{\text{ph}C}$) and V (V') the value V_C (V'_C). Neglecting I_0 and I'_0 with respect to $I_{\text{ph}C}$, we can write from Eqs. (A1) and (A2),

$$I_{\text{ph}C} = I_C - I_{dC} - V_C/R, \quad (\text{A13})$$

$$V'_C = V'_A - (n'kT/e)\ln(I_A/I_C), \quad (\text{A14})$$

and then

$$V_C = R(I_A - I_{dA}) - (n'kT/e)\ln(I_A/I_C). \quad (\text{A15})$$

Finally we obtain

$$I_{\text{ph}C} = (I_C - I_A) - (I_{dC} - I_{dA}) + (n'kT/eR)\ln(I_A/I_C). \quad (\text{A16})$$

In this last calculation, we have only neglected I_0 and I'_0 . The result is therefore correct over almost the whole voltage (or current) range, in fact as soon as I_A is not too small when compared with I_C (which is the case of the points that we have chosen where $U_A = U_C = -0.7$ V, $I_A = -0.056$ mA, and $I_C = 0.362$ mA). Note that, in Eq. (A15), $I_{dC} - I_{dA}$ can be neglected: $U_A = U_C$ is low enough that I_{dC} and I_{dA} are only very small fractions of I_C ; moreover, after Eqs. (A11) and (A15),

$$V_A - V_C \approx (n'kT/e)\ln(I_A/I_C)$$

is small, so that I_{dC} and I_{dA} are of the same order. Then we obtain $I_{\text{ph}C} \approx I_C - I_A \approx 0.330$ mA.

4. Estimation of n

As we said before, we first neglect the weak variation of I_{ph} over the voltage range chosen for the analysis. Then, $I_{\text{ph}}(0)$ being the value of I_{ph} when $V=0$, we assume that $I_{\text{ph}} = I_{\text{ph}}(0) = I_{\text{ph}C}$. We choose on the $I(U)$ curve recorded *under light excitation* a particular point D of coordinates (U_D, I_D) so that $0 < -I_D < -I_{\text{ph}}$ (Fig. 14). At this point, the value V_D of the bias is positive (remark that, consequently, $I_{dD} = 0$). Then, we are interested in a part of the characteristics where the current variation is dominated by the exponential term in Eq. (A1). Therefore, the slope of the $I(U)$ curve at point D , $Y_D = (dI/dU)_D$, should strongly depend on the value of n . Neglecting I_0 and I'_0 we differentiate Eqs. (A1), (A2), and (A3) and we get

$$Y_D = \{ (e/nkT)(I_D - I_{ph} - V_D/R) + 1/R \} \\ \times \{ 1 + (n'kT/eI_D)Y_D \}. \quad (A17)$$

We consider now the point B of the $I(U)$ curve recorded in the dark of coordinates (U_B, I_B) such that $I_B = I_D$ (as drawn in Fig. 14 for simplicity, the points B and D may be chosen so that B coincides with A). Then, we can write

$$V_D \approx U_D - U_B + RI_D(1 - I_{dB}/I_D). \quad (A18)$$

Combining Eqs. (A17) and (A18), and neglecting I_{dB}/I_{ph} with respect to unity, we obtain

$$n/n' = [(U_B - U_D)/RI_D][1 - RI_{ph}/(U_B - U_D)] \\ \times (1 + \beta_D/Y_D)/(1 - 1/\beta_D R - 1/Y_D R), \quad (A19)$$

where $\beta_D = eI_D/n'kT$. As n/n' should be of the order of unity, a reliable determination of n after Eq. (A19) is obtained when the factors in this expression of n/n' are all of the same order, which occurs for $-0.35 < U_D < -0.25$ V (i.e., when $I \approx I_{ph}/2$). In this domain, Eq. (A19) yields $nkT/e \approx 0.027$ V.

5. Estimation of V_{oc} and V_{oc}^*

We show now that V_{oc} and V_{oc}^* can be graphically determined. We consider the points E and H where the U axis intercepts the tangents to the $I(U)$ curves, respectively, at point A and at point D (Fig. 14). Their coordinates are $(U_E, 0)$ and $(U_H, 0)$. Starting from Eqs. (A6)–(A8) and (A17), we calculate U_E and U_H , again assuming that I_{ph} is constant when $0 \leq V \leq V_{oc}^*$:

$$U_E = U_A - RI_A[1 - R\alpha_A/(1 + R\alpha_A)] + n'kT/e, \quad (A20)$$

$$V_{oc}^* \approx U_H - U_E + RI_D[R\alpha_A/(1 + R\alpha_A) - I_d/I_D]$$

$$- (nkT/e) \{ \ln[1 + (U_D - U_A - RI_{dA} - V_{oc}^*)/(RI_{ph}(0) + V_{oc}^*)] + RI_D/[RI_{ph}(0) - RI_d + U_D - U_A - nkT/e] \}. \quad (A26)$$

It is easy to check that at the points A and D that we have chosen, $U_H - U_E$ is much larger than all of the other terms in the expression of V_{oc}^* . Then, by simply measuring the distance between the points E and H (see Fig. 14), we can deduce a good estimate of V_{oc}^* :

$$V_{oc}^* \approx U_H - U_E \approx 0.265 \text{ V}. \quad (A27)$$

6. Estimation of I_0 and I_0'

The above value of V_{oc}^* can be used to estimate I_0' from Eq. (A5) and I_0 from Eqs. (A22) and (A25). We find $I_0' = 1.8 \times 10^{-7}$ mA and $I_0 = 1.4 \times 10^{-5}$ mA.

$$U_H = U_D + n'kT/e \\ - (nkT/e) \{ 1/[1 - I_{ph}(0)/I_D \\ - (V_D - nkT/e)/RI_D] \}. \quad (A21)$$

We can define the open-circuit voltage V_{oc} as the polarization of \mathcal{D} when the current that would cross the junction *in the dark* will be opposite of the internal photocurrent $I_{ph}(0)$:

$$I_{ph}(0) = -I_0[\exp(eV_{oc}/nkT) - 1]. \quad (A22)$$

Neglecting I_0 , the current-voltage Eq. (A1) at point D may be written

$$I_D/I_{ph}(0) \approx -\exp[(eV_D - eV_{oc})/nkT] \\ + 1 + V_D/RI_{ph}(0), \quad (A23)$$

and we get

$$V_{oc} \approx V_D - (nkT/e) \ln[1 - I_D/I_{ph}(0) + V_D/RI_{ph}(0)]. \quad (A24)$$

In fact, we are more specifically interested in calculating the effective open-circuit voltage V_{oc}^* , which takes into account the load resistance R . Simply writing the current-voltage Eq. (A1) at the point of coordinates $(V_{oc}^*, 0)$ of the $I(U)$ curve recorded *under light excitation*, we obtain

$$V_{oc}^* \approx V_{oc} - (nkT/e) \ln\{1/[1 + V_{oc}^*/RI_{ph}(0)]\}. \quad (A25)$$

Using Eq. (A18) (where we replace point B by point A), we calculate V_D and we get

7. Determination of V versus U

At this point of the calibration procedure, we have made good estimations of the relevant parameters of our modeled system. We now calculate from the experimental $I(U)$ curves the approximate current-voltage characteristics of each component of the equivalent circuit and deduce the variation of I_d and I_{ph} versus V .

Note that the dependence of I_{ph} versus V is given by³²

$$I_{ph} = I_\phi [1 - \exp(-aw)/(1 + a\ell)], \quad (A28)$$

where I_ϕ , a constant proportional to the light power, would be the internal photocurrent if all the light absorption by the semiconductor only occurred inside of the BB

region, α is the optical-absorption coefficient, ℓ is the electron diffusion length,

$$w = w_0[(V + V_B)/V_B]^{1/2}$$

is the BB width when the bias V is applied to the junction [w_0 and V_B are calculated and measured (see Secs. II and III C 2 (a) of the main text)]. Then, we have

$$\ln[1/(1 - I_{\text{ph}}/I_{\phi})] = \alpha w + \ln(1 + \alpha\ell). \quad (\text{A29})$$

We plot $\ln[1/(1 - I_{\text{ph}}/I_{\phi})]$ versus w , using the experimental variation of I_{ph} versus V . As predicted by Eq. (A29), we indeed obtain a straight line of slope $\alpha \approx 0.7 \mu\text{m}^{-1}$ which confirms that, in the voltage range that we use to perform FA-photoemission experiments, at least 65% of the light is absorbed in the bulk of the semiconductor crystal. From the extrapolation of the line to $w=0$ (i.e., to $V = -V_B$) we obtain $1 + \alpha\ell \approx 2.4$, i.e., $\ell \approx 2.1 \mu\text{m}$.

Now, for a given value of V , we calculate, with Eq. (A1), the corresponding value of I . From Eq. (A2), we deduce the value of V' and Eq. (A3) determines U . By varying V , we build a voltage-calibration curve which associates to each measured value of U the corresponding value of V , i.e., the BB amplitude. The characteristics calculated after this calibration procedure (symbol + in Fig. 5) fit very well the experimental $I(U)$ curves.

Accounting for the variation of I_d and I_{ph} versus V , we have calculated corrected values of the equivalent circuit parameters which are not very significantly changed, as can be seen in the case of R (Sec. 2 of this appendix). Using this set of parameters, we obtain the very good fit of the experimental $I(U)$ curves shown in Fig. 5. It must be also noted that, when we consider $I_{\text{ph}} = I_{\text{ph}}(0)$ and $I_d = 0$, the shape of the characteristics that we calculate is quite affected because, when $-3 < U < 0$ V, I_d actually varies from -0.6 to 0 mA and I_{ph} from -0.38 to -0.33 mA, but the error made on V [i.e., on $e(V + V_B)$] over this entire voltage range is at most 12 mV (i.e., half of our experimental resolution) because at large current the voltage drop at the back contact remains nearly constant.

APPENDIX B: POLAR-OPTICAL-PHONON COLLISION TIME

Among the different scattering mechanisms, the collisions with polar optical phonons are largely the most

$$I(\mathbf{k} + \mathbf{q}) = \int_{\theta=0}^{\pi} \delta(\varepsilon' - \varepsilon + \hbar\omega) \sin\theta d\theta = \frac{m_6}{\hbar^2 k q} \quad \text{for } k[1 - (1 - \hbar\omega_{\text{op}}/\varepsilon)^{1/2}] \leq q \leq k[1 + (1 - \hbar\omega_{\text{op}}/\varepsilon)^{1/2}], \quad (\text{B3})$$

$$I(\mathbf{k} + \mathbf{q}) = 0 \quad \text{out of this } q \text{ range.} \quad (\text{B4})$$

Considering the polar-optical-phonon energy $\hbar\omega_{\text{op}}$ as independent of q , the summation over q leads to the expression of the emission rate for electrons of kinetic energy $\varepsilon \geq \hbar\omega_{\text{op}}$:²⁷

$$1/\tau_{\text{op}} = (1/\tau_0)(\hbar\omega_{\text{op}}/\varepsilon)^{1/2} \sinh^{-1}[(\varepsilon/\hbar\omega_{\text{op}}) - 1]^{1/2}, \quad (\text{B5})$$

efficient relaxation processes for electrons of low kinetic energy (i.e., in the vicinity of the Γ_6 minimum of the conduction band) in p -type III-V semiconductor compounds of moderate doping level. As we are interested in transport mechanisms occurring at quite low lattice temperature (about 120 K), we only consider here phonon emission which is much more probable than phonon absorption in this temperature range. We calculate the scattering rate for polar-optical-phonon emission following the treatment of Conwell²⁷ but in the framework of a conduction-band description,^{12,29} deduced from the Kane model,²⁸ which accounts for nonparabolicity. This treatment is also related to Zawadski's approach.³³

In high-mobility materials, electron-phonon interaction may be treated by perturbation theory. Then, the probability per unit time w_{if} of a transition by emission of a phonon of energy $\hbar\omega$ and wave vector \mathbf{q} between states of kinetic energy and wave vector ε, \mathbf{k} and $\varepsilon' = \varepsilon - \hbar\omega$, $\mathbf{k}' = \mathbf{k} + \mathbf{q}$ is given by (in this appendix vectors are designated by boldface characters, their moduli by plain characters)

$$w_{\text{if}} = (2\pi/\hbar) |H'_{\text{if}}|^2 \delta(\varepsilon' - \varepsilon + \hbar\omega), \quad (\text{B1})$$

where H'_{if} is the matrix element of the interaction potential between the initial and final states and the δ function accounts for energy conservation.

Then the scattering rate corresponding to phonon emission can be written

$$\frac{1}{\tau} = \frac{2\pi}{\hbar} \int_{q=0}^{+\infty} \int_{\theta=0}^{\pi} \int_{\phi=0}^{2\pi} \frac{v}{(2\pi)^3} |H'_{\text{if}}|^2 \times \delta(\varepsilon' - \varepsilon + \hbar\omega) q^2 \sin\theta d\theta d\phi dq, \quad (\text{B2})$$

where v is the crystal volume and q the modulus of the phonon wave vector. Here the summation is performed over the spherical coordinates, q, θ, ϕ with the \mathbf{k} direction taken as the z axis.

Usually the scattering rate $1/\tau_{\text{op}}$ relevant to polar-optical-phonon emission is calculated for carriers with wave functions of s symmetry in a parabolic conduction band of effective mass m_6 . In this case, the matrix element $|H'_{\text{if}}|$ of the perturbing potential depends on \mathbf{q} only through its modulus $|H'_{\text{if}}|^2 = D/q^2$, where D is a constant. Then, the integration over θ can be first carried out and yields²⁷

where τ_0 is a characteristic time constant.

Let us now assume that the variation of the electron wave-vector modulus $\Delta k = k' - k$ is small when compared to k . Then we can write

$$\varepsilon' - \varepsilon \approx \nabla_{\mathbf{k}} \varepsilon \cdot \Delta \mathbf{k}, \quad (\text{B6})$$

where $\Delta \mathbf{k} = \mathbf{q}$. From this expression we obtain for an iso-

tropic conduction band

$$\varepsilon' - \varepsilon + \hbar\omega \approx \hbar v_G q [\cos\theta + q/2k] + \hbar\omega. \quad (\text{B7})$$

It is therefore clear that, contrary to Eq. (B5), the expression of $1/\tau_{\text{op}}$ that will be obtained using Eq. (B7) after integration over θ and q will not depend explicitly on ε but on the electron group velocity v_G and k .

When taking into account the conduction-band non-parabolicity, it is also necessary to consider conduction wave functions which are not of s symmetry which introduces an angular dependence in the matrix element $|H'_{if}|$. We will use the definition of the wave-function coefficients a_6 , b_6 , and c_6 of the conduction states given by Kane in a $\mathbf{k}\cdot\mathbf{p}$ perturbation model of the band structure.²⁸ These coefficients describe the band hybridization. As shown in Ref. 29, when the spin-orbit coupling energy Δ is smaller than the band-gap energy E_G (which is the case for InP), it is a very good approximation to write

$$a_6^2 = 1 - c_6^2 \quad \text{and} \quad b_6^2 = 0. \quad (\text{B8})$$

In the framework of this approximation, following the treatment of Fawcett, Boardmann, and Swain,³⁴ the matrix element of the perturbing potential can be simply written

$$|H'_{if}|^2 = (D/q^2)[a_6^2 + c_6^2 \cos^2\theta']^2, \quad (\text{B9})$$

where θ' is the angle between \mathbf{k} and \mathbf{k}' .

Using Eqs. (B8), we obtain

$$|H'_{if}|^2 = (D/q^2)[1 - 2c_6^2(1 - c_6^2)(1 - \cos\theta') - (2c_6^4/3)3(1 - \cos^2\theta')/2]. \quad (\text{B10})$$

For small kinetic energies, i.e., small values of k , c_6^2 is much smaller than a_6^2 (i.e., $a_6^2 \approx 1$ and $c_6^2 \approx 0$). Then, the terms proportional to c_6^2 in Eq. (B10) yield significant contributions in the expression of the scattering rate when Δk is much smaller than k , i.e., $k \approx k'$. In this case we can use in Eq. (B10) the relation

$$1 - \cos\theta' \approx 2 \cos^2\theta. \quad (\text{B11})$$

According to Eq. (B7), from energy conservation we obtain

$$1 - \cos\theta' \approx 2[(q/2k) + (\hbar\omega_{\text{op}}/\hbar v_G q)]^2. \quad (\text{B12})$$

Then the scattering rate is given by

$$1/\tau_{\text{op}} = 1/\tau_0 - 2c_6^2(1 - c_6^2)(1/\tau_1) - (2c_6^4/3)(1/\tau_2), \quad (\text{B13})$$

where

$$\frac{1}{\tau_0} = \frac{1}{\tau^*} \frac{\mathcal{P}}{\hbar v_G} \int_{q_0}^{q_1} \frac{1}{q} dq, \quad (\text{B14})$$

$$\frac{1}{\tau_1} = \frac{1}{\tau^*} \frac{\mathcal{P}}{\hbar v_G} \int_{q_0}^{q_1} \frac{1}{q} \left[\frac{q}{2k} + \frac{\hbar\omega_{\text{op}}}{\hbar v_G q} \right]^2 dq, \quad (\text{B15})$$

$$\frac{1}{\tau_2} = \frac{1}{\tau^*} \frac{\mathcal{P}}{\hbar v_G} \int_{q_0}^{q_1} \frac{3}{q} \left[\frac{q}{2k} + \frac{\hbar\omega_{\text{op}}}{\hbar v_G q} \right]^2 \times \left[1 - \left[\frac{q}{2k} + \frac{\hbar\omega_{\text{op}}}{\hbar v_G q} \right]^2 \right] dq. \quad (\text{B16})$$

The quantity \mathcal{P} is the real momentum matrix element between valence and conduction states defined by Kane,²⁸ the boundaries of the integration over q are

$$q_0 = k[1 - (1 - \hbar\omega_{\text{op}}/\varepsilon)^{1/2}]$$

and

$$q_1 = k[1 + (1 - \hbar\omega_{\text{op}}/\varepsilon)^{1/2}].$$

These expressions are obtained after the summation over θ :

$$I(\mathbf{k} + \mathbf{q}) = \int_{\theta=0}^{\pi} \delta \left\{ \hbar v_G q \left[\cos\theta + \frac{2k}{q} \right] + \hbar\omega \right\} \sin\theta d\theta = \frac{1}{\hbar v_G q}. \quad (\text{B17})$$

The last two terms in Eq. (B10) are, respectively, proportional to $P_1(1) - P_1(\cos\theta')$ and to $P_2(1) - P_2(\cos\theta')$, P_1 and P_2 being the first and second Legendre polynomials. Then, in the case where hybridization is not considered, $1/\tau_1$ and $1/\tau_2$ also describe the relaxation of the anisotropic part of the distribution, while $1/\tau_0$ is the scattering rate which differs from the expression of Eq. (B5) by the fact that the variable which appears explicitly is $\hbar v_G k$ instead of ε .

As mentioned before, the terms which depend on c_6^2 in the expression of $1/\tau_{\text{op}}$ [Eq. (B13)] are of significant order of magnitude when the kinetic energy is not too small. Then, assuming that this is the case when $(\hbar\omega_{\text{op}}/\hbar v_G k)$ is small with respect to unity, among these contributions we only retain, after integration over q , those proportional to $(1 - 2\hbar\omega_{\text{op}}/\hbar v_G k)^{1/2}$, which ensure that the final formula remains a good approximation of $1/\tau_{\text{op}}$ close to the zone center. In the framework of this assumption, $1/\tau_1$ and $1/\tau_2$ are given by

$$1/\tau_1 \approx \frac{2}{3}(1/\tau_2) \approx (1/\tau^*)(\mathcal{P}/\hbar v_G)(1 - 2\hbar\omega_{\text{op}}/\hbar v_G k)^{1/2}, \quad (\text{B18})$$

and, finally, we obtain

$$1/\tau_{\text{op}} = (1/\tau^*)(\mathcal{P}/\hbar v_G) \times \{ \sinh^{-1}[(\hbar v_G k/2\hbar\omega_{\text{op}}) - 1]^{1/2} - 2c_6^2(1 - c_6^2/2)(1 - 2\hbar\omega_{\text{op}}/\hbar v_G k)^{1/2} \}. \quad (\text{B19})$$

In order to solve numerically the transport equation in Sec. VB of the main text, we have used approximate expressions of the kinetic energy ε and wave-function coefficients a_6 , b_6 , and c_6 of the conduction band given in Ref. 29:

$$\begin{aligned}\varepsilon &= -\mathcal{E}_{\text{eff}}^*/2 + \mathcal{E}_1, \\ a_6^2 &= (1 - c_6^2) = \frac{1}{2}(1 + \mathcal{E}_{\text{eff}}^*/2\mathcal{E}_1),\end{aligned}\quad (\text{B20})$$

where $\mathcal{E}_{\text{eff}}^* = E_G + \Delta/3$ and

$$\mathcal{E}_1 = [(\mathcal{E}_{\text{eff}}^*/2)^2 + (k\mathcal{P})^2]^{1/2}.$$

Using Eqs. (B20), it is readily shown that Eq. (B7) still holds when $\Delta k \approx k$. It is also clear that the terms depending on c_6^2 are of significant order of magnitude only when $\hbar v_G k$ is several times larger than $\hbar\omega_{\text{op}}$. Then the expression of the polar-optical-phonon emission rate given by Eq. (B19) is valid all over the central Γ valley, including the low-energy range.

- ¹See, for instance, D. J. Bartelink, J. L. Moll, and N. I. Meyer, *Phys. Rev.* **130**, 972 (1963).
- ²J. Scheer and J. Van Laar, *Solid State Commun.* **3**, 189 (1965).
- ³T. Itoh, I. Matsuda, K. Hasegawa, and K. Umeoka, *J. Appl. Phys.* **38**, 3395 (1967).
- ⁴T. Itoh, I. Matsuda, and K. Hasegawa, *J. Appl. Phys.* **41**, 1945 (1970); T. Itoh, *ibid.* **41**, 1951 (1970).
- ⁵I. Shariary, J. R. Schwank, and F. G. Allen, *J. Appl. Phys.* **50**, 1428 (1979).
- ⁶R. L. Bell, L. W. James, and R. L. Moon, *Appl. Phys. Lett.* **25**, 645 (1974); T. J. Maloney, M. G. Burt, J. S. Escher, P. E. Gregory, S. B. Hyder, and G. A. Antypas, *J. Appl. Phys.* **51**, 2879 (1980).
- ⁷J. S. Escher, P. E. Gregory, and T. J. Maloney, *J. Vac. Sci. Technol.* **16**, 1394 (1979).
- ⁸J. S. Escher, in *Semiconductor and Semimetals*, edited by R. K. Willardson and A. C. Beer (Academic, New York, 1981), Vol. 15, p. 195.
- ⁹H.-J. Drouhin, C. Hermann, and G. Lampel, *Phys. Rev. B* **31**, 3859 (1985).
- ¹⁰H.-J. Drouhin, C. Hermann, and G. Lampel, *Phys. Rev. B* **31**, 3872 (1985).
- ¹¹J. Peretti, H.-J. Drouhin, and D. Paget, *Phys. Rev. Lett.* **64**, 1682 (1990).
- ¹²J. Peretti, H.-J. Drouhin, D. Paget, and A. Mircéa, *Phys. Rev. B* **44**, 7999 (1991).
- ¹³J. S. Escher, R. D. Fairman, G. A. Antypas, R. Sankaran, L. W. James, and R. L. Bell, *Crit. Rev. Solid State Sci.* **5**, 577 (1975).
- ¹⁴J. S. Escher, R. L. Bell, P. E. Gregory, S. B. Hyder, T. J. Maloney, and G. A. Antypas, *IEEE Trans. Electron Devices* **ED-27**, 1244 (1980).
- ¹⁵W. J. Turner, W. E. Reese, and G. D. Pettit, *Phys. Rev.* **136**, A1467 (1964).
- ¹⁶C. Piaget, Thèse de Doctorat d'Etat, Université de Paris-Sud, Centre d'Orsay, 1982.
- ¹⁷I. A. Babalola, W. G. Petro, T. Kendelewicz, I. Lindau, and W. Spicer, *Phys. Rev. B* **29**, 6614 (1984).
- ¹⁸P. Maigne, C. A. Sebenne, and A. Taleb-Ibrahimi, *Surf. Sci.* **162**, 663 (1985).
- ¹⁹H.-J. Drouhin and M. Eminyan, *Rev. Sci. Instrum.* **57**, 1052 (1986).
- ²⁰E. Bedel, G. Landa, R. Carles, J.-P. Redoulès, and J.-B. Renucci, *J. Phys. C* **19**, 1471 (1986).
- ²¹R. H. Fowler, *Phys. Rev.* **38**, 45 (1931).
- ²²E. H. Rhoderick, *Metal-Semiconductor Contacts*, edited by P. Hammond and D. Walsh (Oxford University, Oxford, 1978).
- ²³M. Alonso, R. Cimino, and K. Horn, *Phys. Rev. Lett.* **64**, 1947 (1990).
- ²⁴L. W. James, J. P. Van Dyke, F. Herman, and D. M. Chang, *Phys. Rev. B* **1**, 3998 (1970).
- ²⁵W. E. Spicer and R. C. Eden, in *Proceedings of the Ninth ICPS, Moscow, 1968*, edited by S. M. Ryvkin and Yu. V. Schmartsev (Nauka, Leningrad, 1968), p. 65.
- ²⁶J.-N. Chazalviel (private communication); band-structure calculation after M. L. Cohen and T. K. Bergstresser, *Phys. Rev.* **141**, 789 (1966).
- ²⁷E. M. Conwell, *Solid State Physics: High-Field Transport in Semiconductors, Suppl. 9*, edited by F. Seitz, D. Turnbull, and H. Ehrenreich (Academic, New York, 1967), and references therein.
- ²⁸E. O. Kane, *J. Phys. Chem. Solids* **1**, 249 (1957).
- ²⁹H.-J. Drouhin and J. Peretti, *Phys. Rev. B* **44**, 7993 (1991).
- ³⁰J.-Y. Bigot, M. T. Portella, R. W. Schoenlein, J. E. Cunningham, and C. V. Shank, *Phys. Rev. Lett.* **65**, 3429 (1990).
- ³¹R. G. Ulbrich, J. A. Kash, and J. C. Tsang, *Phys. Rev. Lett.* **62**, 949 (1989); J. Shah, B. Deveaud, T. C. Damen, W. T. Tsang, A. C. Gossard, and P. Lugli, *ibid.* **59**, 2222 (1987), and references therein.
- ³²S. M. Sze, *Physics of Semiconductors Devices* (Wiley, New York, 1969).
- ³³W. Zawadzki, *Handbook of Semiconductors*, edited by T. S. Moss (North-Holland, Amsterdam, 1982), Vol. 1, edited by W. Paul, p. 713.
- ³⁴W. Fawcett, A. D. Boardman, and S. Swain, *J. Phys. Chem.* **31**, 1963 (1970).